Journal of the Mechanical Behavior of Biomedical Materials 72 (2017) 90–101

Contents lists available at ScienceDirect

Journal of the Mechanical Behavior of Biomedical Materials

journal homepage: www.elsevier.com/locate/jmbbm

# Characterizing viscoelasticity of unhydrolyzed chicken sternal cartilage extract suspensions: Towards development of injectable therapeutics formulations

Brian Hama, Gautam Mahajan, Chandrasekhar Kothapalli*

*Department of Chemical and Biomedical Engineering, Cleveland State University, Cleveland, OH 44115, USA*

ARTICLE INFO

*Keywords:*
Cartilage extract
Unhydrolyzed type II collagen
Rheology
Viscoelasticity
Models

ABSTRACT

Exogenous delivery of cartilage extract is being explored as a promising candidate for knee arthritis treatment as it biomimics native cartilage tissue characteristics. In this study, we report on the rheological characterization of aqueous suspensions constituted from a powdered form of unhydrolyzed chicken sternum extract. The effect of particle size (as-received vs. milled), suspension fluid (water vs. PBS), and temperature (37 °C vs. 4 °C), on the viscoelastic properties of the sternum extract based particulate suspensions were evaluated. Results showed that these suspensions exhibit shear-thinning characteristics as shear rate ($\dot{\gamma}$) increases, while viscosity ($\eta$), storage ($G'$), and loss ($G''$) moduli of the suspensions increased with increasing particulate loading ($\phi$: 2.5–10 wt%). Reducing the as-received particle size by milling decreased G′, G⌓, and $\eta$ of the suspensions and increased the influence of $\phi$ on these properties, possibly due to improved particle packing. Replacing water with PBS had no significant effect on the rheological properties, but temperature reduction from 37 °C to 4 °C increased $G'$, $G''$, and $\eta$ of the suspensions and lowered the impact of powder loading on viscoelastic properties. The suspension's time-dependent response was typical of viscoelastic materials, characterized by an asymptotical approach to a final stress (stress relaxation) or strain (creep). Results were fit to a power-law model for creep, a general relaxation model for exponential decay in stress, Carreau-Yasuda models for flow curves, and a two-parameter Liu model to identify the maximum powder loading ($\phi_m$). Among the various forces involved in particle-particle interactions within these suspensions, electrostatic forces appeared to dominate the most. Such characterization of the viscoelastic nature of these suspensions would help in formulating stable injectable cartilage extract based therapeutics for *in vivo* applications.

## 1. Introduction

Colloidal suspensions of synthetic and biological polymers have become of great interest in recent years for biomedical applications (Abdelhamid and Elaissari, 2003; Jeong et al., 2002; Kadajji and Betageri, 2011; Klouda and Mikos, 2008; Li et al., 2012; Stainmesse et al., 1995; Ulery et al., 2011). The utility of such suspensions in joints could significantly alter the way knee arthritis is treated (Kim et al., 2011; Reddi et al., 2011; Sheu et al., 2013). When the knee joint is subjected to compressive loading, the articular cartilage in the joint absorbs and dissipates energy, facilitates load-transfer, provides cushion to prevent direct bone-on-bone grinding, and enables comfortable joint movement. Articular cartilage could degrade due to trauma, mechanical injury, inflammation, or general wear, leading to the formation of fissures and reduced mechanical stability (Waldstein et al., 2016). Under such conditions, water retention ability of cartilage is compromised resulting in the loss of joint cushion, contributing to the pain and discomfort experienced by arthritis patients. In lieu of drugs or invasive surgery, replacing the degenerated cartilage to restore cushioning and mechanical stability is being increasingly explored. This could partially be achieved by delivering cartilage extract directly in the affected area to minimize biological incompatibility or undesirable mechanical mismatch in the joint.

The biological and mechanical properties of articular cartilage and its primary constituents have been reported earlier. Extracellular matrix (ECM) forms 10–30% by weight of the articular cartilage, and consists predominantly of type II collagen, proteoglycans and other macromolecular proteins (Ma and Langer, 1999; Mow et al., 1984). The collagen network not only tempers the tensile and compressive stiffness of cartilage but also regulates the fluid pressure within (Korhonen et al., 2003; Mononen et al., 2011). Injectable tyramine-modified HA hydrogels (e.g., Synvisc-One®) have been reported to be a potentially viable

* Corresponding author.
*E-mail address:* c.kothapalli@csuohio.edu (C. Kothapalli).

http://dx.doi.org/10.1016/j.jmbbm.2017.04.025
Received 6 February 2017; Received in revised form 16 April 2017; Accepted 25 April 2017
Available online 26 April 2017
1751-6161/ 

substitute scaffold for rheumatoid arthritis (Kim et al., 2011). Hydrogels based on aldehyde hyaluronan and adipic dihydrazide hyaluronan combined with the inhibitor ADAMTS-5 have been shown to be capable of retarding cartilage degradation and promoting its repair (Chen et al., 2014). It has also been reported that *in vitro* expanded human meniscus-derived cells in 3D bioresorbable PGA-hyaluronan scaffolds can be used to repair meniscus tissue (Freymann et al., 2012). However, these materials are devoid of type II collagen – a critical component of cartilage ECM.

Numerous patents have been filed in recent years highlighting the potential utility of collagen based extracts for applications in cartilage tissue replacement. Examples include, a hydrolyzed collagen type II from chicken sternum cartilage (Ishaq, 2006), a hyaluronic acid and chondroitin sulfate based collagen extract, Kolla2 cartilage powder (Stiles, 2002), hydrolyzed collagen type II powders (Alkayali, 2000, 2001), avian cartilage hydrolysate (Vouland and Berger, 2010), self-assembled-peptide hydrogels (Harris et al., 2011), and hydrogels consisting hyaluronic acid and phosphatidyl ethanolamine (Kitazono et al., 2008). In addition to applications in joint health, such collagen powder suspensions were also promoted as dietary supplements and as additives in consumable products and formulations (e.g., improve texture, water-holding capacity). However, the viscoelastic characterization of ECM-based unhydrolyzed collagenous particulate suspensions remains categorically unexplored. Such information is critical from an applications standpoint as it is beneficial to understand the (a) maximum amounts of these powders that could be loaded in a suspension without significant agglomeration, (b) role of delivery platform for injecting this particulate composition at the desirable location, (c) stability of these suspensions in the short- and long- terms, i.e., storage in clinic prior to injection and post-injection in the body, (d) ideal temperatures for maintaining stable suspensions of this powder, and (e) how these suspensions could be physically or chemically manipulated to ensure long-term stability without phase separation.

Although these are quite a few aspects to investigate and therefore form our long-term goals, in the first step, the objective of this study is to elucidate rheological characteristics of an unmodified aqueous suspension of powdered unhydrolyzed chicken sternal collagenous extract. We investigated the effects of particle size (micron vs. nano-sized), processing temperature (37 °C vs. 4 °C), particulate loading amount ($\phi$: 2.5–10 wt%), and suspension medium (deionized water vs. phosphate buffered saline) on the viscoelastic properties of these suspensions. To our knowledge, such a thorough investigation of the viscoelastic characterization of collagen particles loaded cartilage extract suspensions has not been reported.

## 2. Materials and methods

### 2.1. Cartilage extracted powders and their characterization

Chicken sternum cartilage extract was obtained from InterHealth Nutraceuticals UC-II® (UC-250; Benicia, CA), and consists predominantly of an undenatured type II collagen. These powders were not hydrolyzed that will lead to gelatin formation. Two forms of this powder were characterized: as-received, or after milling to reduce the particle size. The as-received powder was milled in a rotating jar with ball bearings (U.S. Stoneware Long Roll Jar Mill) for 12 h, resulting powder added to either distilled water (DI water) or phosphate buffered saline (1× PBS) to result in 10 wt% suspension, and ultrasonically-treated (15 min at 75% power; QSonica LLC, Newtown, CT) to breakdown the particulate agglomerates. The 10 wt% suspensions of as-received powder as well as milled powder had a pH ≈ 7.3. Both the as-received and milled powders were examined using a MFP-3D-Bio atomic force microscope (AFM; Asylum Research, Santa Barbara, CA) mounted on an inverted optical microscope (NIKON Eclipse Ti), and several images taken at multiple magnifications were processed to determine the particle size distributions of both powder types. To accommodate the low stiffness and avoid sample damage, we modified tip-less AFM cantilevers (model TL-CONT, Asylum Research, 0.2 N/m) by attaching a 4.5 µm polystyrene bead using epoxy. The spring constant was calibrated using thermal calibration method on a clean glass slide. The cantilever with spherical bead was brought in contact with the glass slide and the samples were imaged in contact mode. At least ten AFM images were captured for each powder type for particle size analysis. Zeta potential ($\xi$) of these powder suspensions was determined using a Malvern Zetasizer Nano ZS (Westborough, MA) at 37 °C, with at least three replicates of these measurements for each powder type.

### 2.2. Rheological characterization

The suspensions were characterized using a Physica MCR 301 Rheometer (Anton Paar, Ashland, VA) using a cone and plate geometry (50 mm diameter, 0.1 mm gap) with smooth surfaces. DI water or PBS, commonly used for such suspensions, was tested to identify a suitable suspension medium for these powders. The as-received or milled powder was suspended at 37 °C or 4 °C, at 2.5%, 5%, 7.5% or 10% by weight. These temperatures signify physiological and typical protein storage conditions, respectively. Suspensions (10 wt%) were serially-diluted to achieve lower particle density suspensions. Table 1 shows the runs performed at the indicated settings. Each sample was allowed to rest for 10 min before initiating the respective test to eliminate the effect of sample loading history and minimize transient oscillations. Amplitude sweeps were first done to identify the linear viscoelastic region (LVR) from the $G'$ and $G''$ vs. strain plots. The frequency ($\omega$) sweeps and creep tests (input stress = 3 Pa) were performed in the linear viscoelastic region LVR (Morrison, 2001a). The flow curve and stress-relaxation tests were performed independent of other tests. Stress relaxation tests were performed at a constant 5% strain, where native cartilage is typically tested (Purslow et al., 1997). All rheological runs were performed in triplicate for each powder type at each condition. Data were fit with specific models using SigmaPlot® V.11 (Systat Software, Inc.).

## 3. Results and discussion

### 3.1. Characterization of cartilage extract powders

The particle size of cartilage extract powder, before and after milling, was quantified from representative AFM images shown in Fig. 1. The respective particle size distributions were fit to Normal, Weibull, Gamma, and Lognormal distributions and the respective scale and shape parameters from the fits were shown in Table 2. Based on log-likelihood values, the as-received powder was best described by Weibull and Gamma distributions, whereas the milled powder followed Lognormal distribution. The presence of large particles with a heterogeneous distribution was evident in the as-received powders, while a

**Table 1**
Summary of tests performed on the particulate suspensions and their experimental conditions. Suspensions in distilled water or PBS were tested at similar conditions.

| Test | Specifications | T, °C | Output |
|---|---|---|---|
| Amplitude sweep | Strain: 0.01–100%; $\omega$: 10 rad/s | 37 ± 0.1; 4 ± 0.1 | $G'$ and $G''$ vs. strain ($\gamma$) |
| Frequency sweep | $\omega$: 0.5–100 rad/s; variable strain | 37 ± 0.1; 4 ± 0.1 | $G'$ and $G''$ vs. frequency ($\omega$) |
| Flow curve | Shear rate: 0.001–100 $s^{-1}$ | 37 ± 0.1; 4 ± 0.1 | Viscosity ($\eta$) vs. shear rate ($\dot{\gamma}$) |
| Creep | Stress: 3 Pa; Time: 600 s | 37 ± 0.1; 4 ± 0.1 | Creep compliance ($J$) vs. time |
| Stress relaxation | Strain: 5%; Time: 600 s | 37 ± 0.1; 4 ± 0.1 | Shear stress ($\tau$) vs. time |

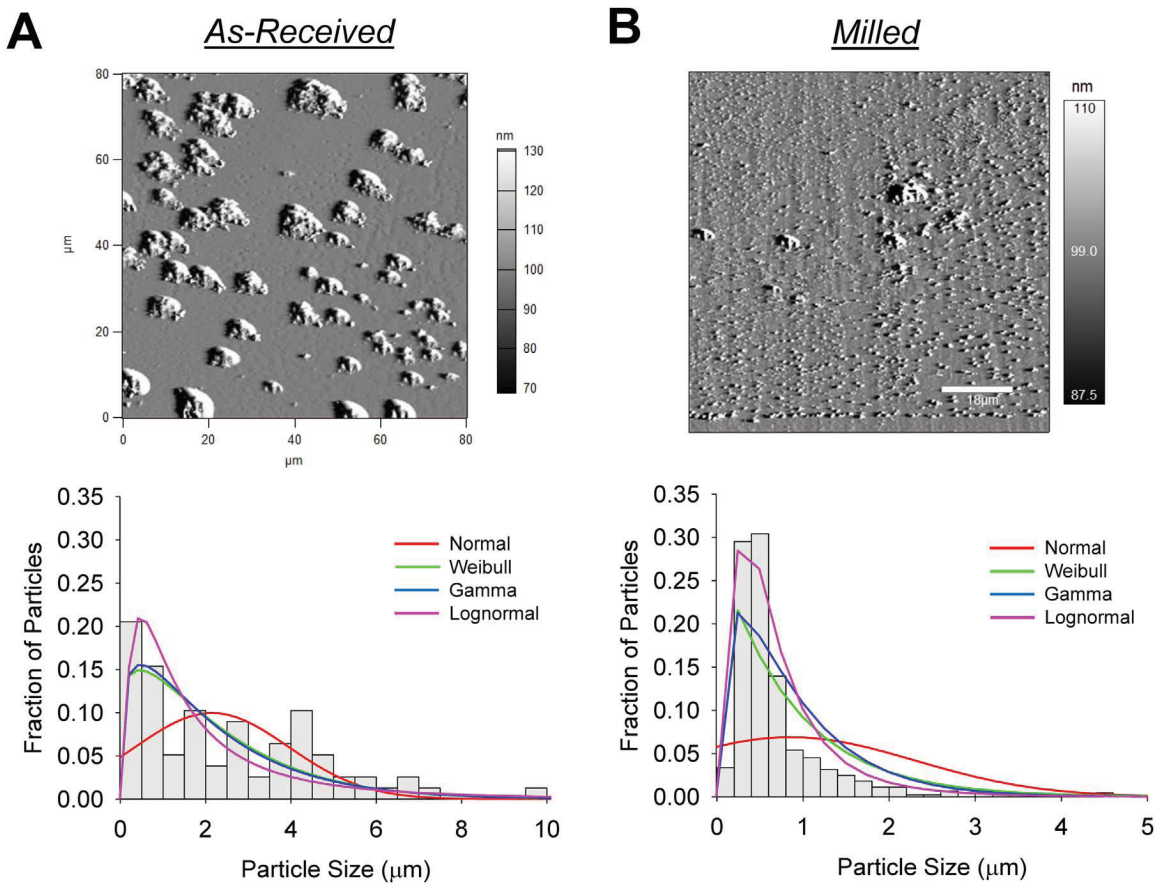


**Fig. 1.** Particle size distributions of the as-received (**A**) and milled (**B**) cartilage extract powders. AFM images obtained from respective samples were quantified by measuring each individual particle size (n > 600 particles in each case) and performing a distribution analysis. The fits of various distributions (Normal, Weibull, Gamma, and Lognormal) were superimposed on the frequency distribution analysis of these powders in each case.

narrow particle size distribution was noted within milled powders with particle sizes in the sub-micron range. A significant reduction in particle size by one order of magnitude ($p < 0.01$ for as-received vs. milled powders) and increased uniformity of particles (narrow distribution) not only demonstrated the effect of milling but also might alter the fluid flow around the particles to ultimately influence the rheological characteristics. The $\xi$ values of the as-received and milled powders were reported in Table 2, and it was noted that the $|\xi|$ of milled particles decreased by 30% upon milling ($p < 0.05$ for as-received vs. milled powders). A negative $\xi$ indicates that the end-groups at the particle surface possess a negative charge while the magnitude relates to suspension stability. Since $\xi \leq -25$ mV for both these particle types, they could be strongly anionic and moderately stable (Clogston and Patri, 2011).

The zeta potential can vary with respect to particle size, temperature, and species of ions in solution (Sze et al., 2003). Although the exact reason for the significant change in zeta potential between as-received and milled powders remains unclear at this stage and will be explored in our future studies, we hypothesize that: (a) the milling and sonication process might have altered the surface chemistry of the as-received powder, or (b) the as-received particles might have an oxidized surface to begin with, compared to milled powder which was always in an aqueous medium, or (c) the sonication process might have induced a modest increase in temperature which could have altered the surface chemistry of milled particles.

### 3.2. Amplitude sweep

Representative results from the amplitude sweeps in aqueous suspensions were shown in Fig. 2. Given the similarities, rheological studies of particle suspensions in PBS were not shown. Here, the data collected from 0.01 − 0.05% strain were omitted due to noise in the signal, typical at low $\gamma$. Results showed that the suspensions were generally slightly elastic (i.e., $G' > G''$) up to 15% strain. Both moduli

**Table 2**
Particle size data for the as-received and milled powders were fitted with Normal, Weibull, Gamma, and Lognormal distributions, and the parameters were listed. For zeta potential measurements, diluted suspensions of each powder in DI water were tested at 37 °C.

| | Normal distribution | | | Weibull distribution | | | Gamma distribution | | | Lognormal distribution | | | Zeta potential (ξ, mV) |
|---|---|---|---|---|---|---|---|---|---|---|---|---|---|
| | Mean (µm) | St. Dev (µm) | Log Likelihood | Scale | Shape | Log Likelihood | Shape | Scale | Log Likelihood | Location | Scale | Log Likelihood | |
| As-received powder | 2.563 | 2.130 | −169.1 | 2.712 | 1.177 | −149.89 | 1.291 | 1.985 | −149.93 | 0.506 | 1.028 | −151.8 | −40.3 |
| Milled powder | 0.863 | 1.443 | −805.0 | 0.871 | 1.015 | −385.0 | 1.386 | 0.623 | −371.3 | −0.549 | 0.743 | −257.5 | −28 |

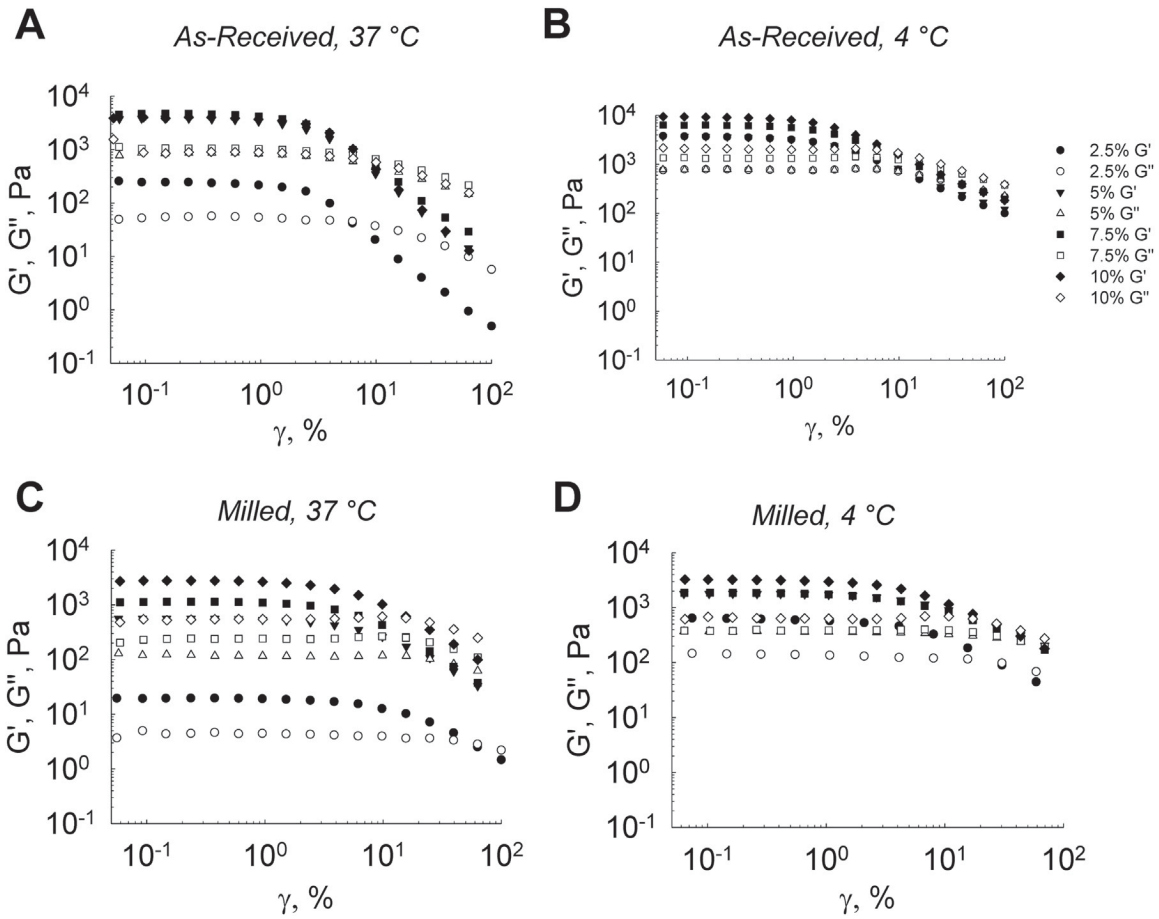


**Fig. 2.** Amplitude sweep results for the as-received powder suspensions in deionized water at 37 °C (**A**) and 4 °C (**B**), and for the milled powder suspensions in deionized water at 37 °C (**C**) and 4 °C (**D**).

decreased sharply starting at ~2% strain, after which $G'$ became slightly lower than $G''$. This behavior is typical for particulate systems, especially in suspensions of clay or abrasive particles (Shukla et al., 2015). The initial plateau with $G' > G''$ might be due to agglomeration or structure formation between the particles, especially at higher loadings. At sufficiently large strains, the structure yields and breaks down, resulting in a sharp decrease in $G'$ to the point where it becomes less than $G''$ and fluidity is restored.

A slight increase in $G''$ curves (slope > 0) with increasing strain was noted in 5 wt% and 7.5 wt% milled powder suspensions at 37 °C (Fig. 2**C**). Such a peak in $G''$ seems common for colloidal suspensions (Krishnaswamy et al., 2009), as it physically arises from an irreversible rearrangement or local yielding of flocculants (Pham et al., 2006). Even in the current study, we noted the tendency of the suspension to flocculate. The absence of such a peak in $G''$ for the 2.5 wt% loading is most likely due to the suspension being too dilute to exhibit this phenomenon. For suspensions with the as-received powder at 37 °C, the larger and less uniform particles probably were less able to form an irreversible arrangement, whereas reducing the temperature possibly assisted with aggregate formation. It could be seen that at all $\phi$, the values of both $G'$ and $G''$ increased when temperature was reduced ($p < 0.05$ for 37 °C vs. 4 °C, at any $\phi$), possibly as a result of this aggregation phenomenon. Both moduli were significantly lower in the milled powder compared to their as-received counterparts ($p < 0.05$ for as-received vs. milled powders, at 37 °C or 4 °C, for any $\phi$), because the smaller particles imposed less frictional resistance to shear.

It was evident in all the cases that both $G'$ and $G''$ increased at higher $\phi$, specifically from 2.5 to 5 wt% loading, characteristic of nanostructured materials such as suspensions of silica nanoparticles (Foudazi and Nazockdast, 2012). Both $G'$ and $G''$ slightly increased at 4 °C, possibly due to higher resistance to motion at lower temperatures. The lower $G'$ and $G''$ values for the milled powder compared to their as-received counterparts could partially be explained by the physical nature of the particles themselves. Being smaller, the milled particles experience less drag and thus offered less resistance to shearing.

### 3.3. Frequency sweep

It was noted from the frequency sweep results (Fig. 3) that $G'$ was always greater than $G''$ at any $\phi$ ($p < 0.05$), and that they both increased slightly with increasing $\omega$ ($p < 0.05$). The suspensions exhibited elastic behavior at low strains, similar to that reported for bovine cartilage (Fulcher et al., 2009), rat tail collagen extracts (Gobeaux et al., 2010), and particulate suspensions and pastes (Burns et al., 2014; Pashkovski et al., 2003; Shukla et al., 2015). Frequency sweep results further support that agglomeration possibly occurred in the suspensions at low strains in the LVR. In a frequency sweep, poroelastic materials with viscoelastic responses such as gels exhibit $G' > G''$, with both $G'$ and $G''$ being independent of $\omega$ (Burns et al., 2014). While the experimental data showed an increase in $G'$ and $G''$ with increasing $\omega$, the dependency was weak, so the behavior of the tested suspensions may be described as poroelastic.

As in the amplitude sweep, the curves for both $G'$ and $G''$ shifted upwards with increasing loading for the same reason described previously. The moduli were in close proximity for the as-received powder, but the curves were more spread out in the case of the milled powder. Furthermore, $G'$ and $G''$ for the milled powder suspensions were considerably lower than those for the as-received powder ($p < 0.05$), and varied by larger amounts as the suspensions become more dilute, especially at 37 °C. This may be explained by the possible

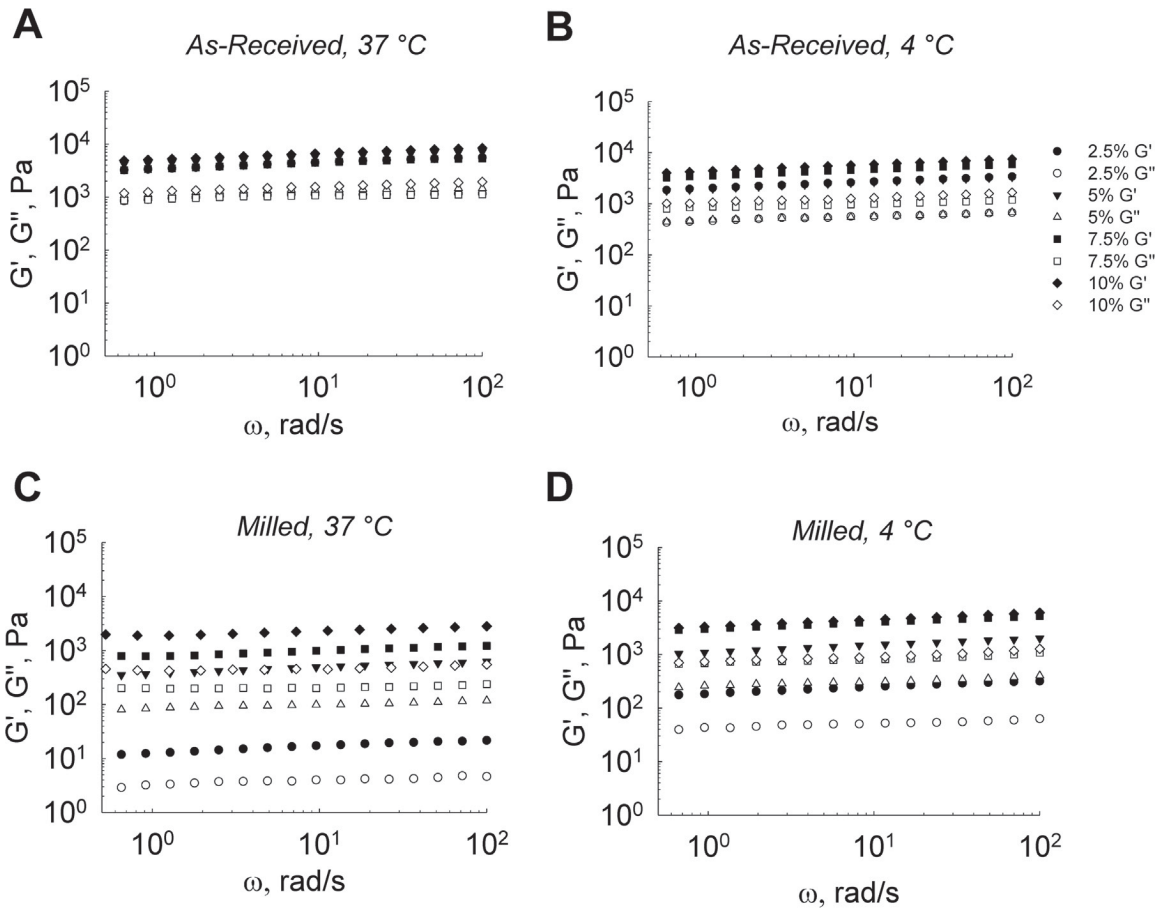


**Fig. 3.** Frequency sweep results for the as-received powder suspensions in deionized water at 37 °C (**A**) and 4 °C (**B**), and for milled powder suspensions in deionized water at 37 °C (**C**) and 4 °C (**D**).

agglomeration formation in suspensions at low temperatures, which partially off-set the effect of powder loading on the magnitudes of $G'$ and $G''$.

### 3.4. Flow curves

The flow curves showed that viscosity peaked at $\dot{\gamma} = 0.002\ s^{-1}$ in all the cases, after which it steadily decreased with increasing $\dot{\gamma}$, indicative of shear-thinning behavior (Fig. 4). Higher viscosity values at low shear rates were likely due to structure formation prior to shearing. Increasing shear rate could have broken the aggregated structures, and liberated fluid that was immobilized within the agglomerates. This resulted in shear-thinning and reduced suspension viscosity with increasing shear rate, at all loadings (Olhero and Ferreria, 2004). The viscosity increased (curve shifting upwards) with increasing $\phi$, especially at 37 °C ($p < 0.05$) independent of particle size, which is to be expected due to higher resistance to flow. The increase in viscosity with higher loading has been well-documented in literature for particulate suspensions of similar particle sizes and shear rates (Prasad and Kytömaa, 1995; Vand, 1948), and agrees with our results. Particulate suspensions are also known to exhibit shear-thinning characteristics, especially when the liquid is of low viscosity, such as water (Konijn et al., 2014). It was noted that at 4 °C, viscosity of the milled powder suspensions were lower than those of the as-received powder suspensions ($p < 0.05$), which could be attributed to a higher packing fraction of the smaller particles in suspension. Similar outcome was reported in a study on silica powder suspensions, which evaluated the effects of milling and sonication on rheological characteristics of powders (Olhero and Ferreria, 2004).

Computer simulations showed that particles whose sizes could be fit with a Normal distribution exhibit higher packing efficiency when the range of sizes is narrower (Shi and Zhang, 2008). In our study, the as-received and milled powders exhibited Weibull (or Gamma) and Lognormal distributions (Fig. 1), respectively, but it was evident that the former had a wider size range, resulting in a lower packing efficiency. The suspension viscosity increased slightly for the as-received powder when the temperature was reduced to 4 °C, but not for milled powder. Higher viscosity at lower temperatures is common for a wide variety of fluids and suspensions, from food products such as fruit juices (Saravacos, 1970) to thermoplastic collagen (Klüver and Meyer, 2012), due to reduced molecular movement (Polachini et al., 2016). Given that the viscosity of water is approximately 0.001 Pa s at room temperature, these particulate suspensions were several orders of magnitude more viscous than water in all cases. Initially, the flow curves data were fit to a simple power-law relationship (Morrison, 2001b) given by Eq. (1):

$$\eta(\dot{\gamma}) = m\dot{\gamma}^{n-1} \tag{1}$$

where $m$ is the consistency index which describes the magnitude of $\eta$, and $n$ is a dimensionless parameter describing the response in viscosity due to increasing $\dot{\gamma}$. While $n = 1$ for Newtonian fluids, $n > 1$ for shear-thickening and $n < 1$ for shear-thinning behaviors. The parameters from the power-law fits were reported in Table 3. It could be seen that $n < 1$ in all cases, indicative of shear-thinning. Although no discernable trend in $n$ values in relation to $\phi$ ($p > 0.1$) were noted, $m$ increased with particulate loading in agreement with the graphical observations. Despite its simplicity and wide usage, a power-law model has limited predictive power. For instance, it is difficult to predict how a similar material of different molecular weight will behave with respect to the tested material (Morrison, 2001b).

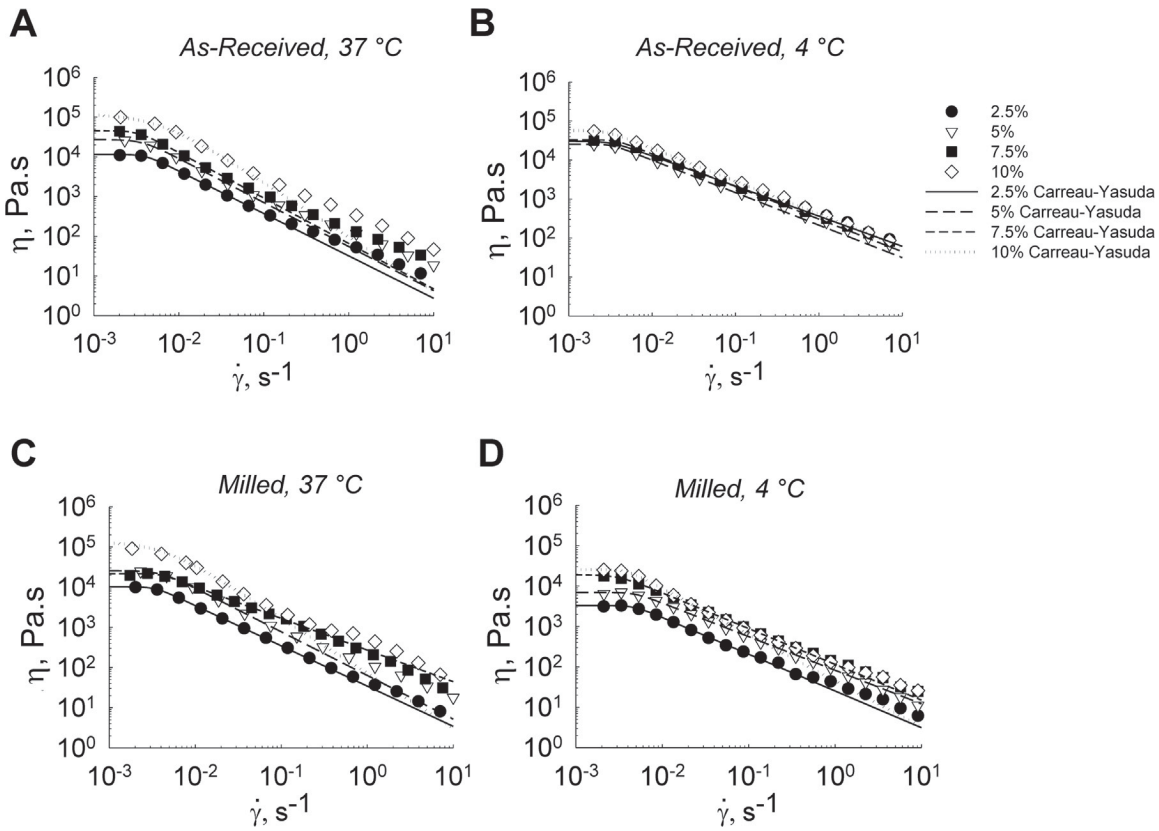


**Fig. 4.** Flow curves of as-received powder suspensions in deionized water at 37 °C (**A**) and 4 °C (**B**), and for milled powder suspensions in deionized water at 37 °C (**C**) and 4 °C (**D**). The experimental data (shown in open and closed symbols) were fit with the Carreau-Yasuda model (Eq. 2) for each particulate loading and the model parameters and statistical significance of the fit were shown in Table 4.

**Table 3**
A power-law model was used to fit the resulting flow curves of the as-received and milled powder suspensions, at various $\phi$ and T, and the calculated parameters $m$ and $n$ tabulated. The overall model fits to the experimental data were significant in each case ($p < 0.008$), with all the model parameters also being significant ($p < 0.05$).

| Condition | $\phi$ (wt%) | $m$ (Pa s) | $n$ |
|---|---|---|---|
| As-received, 37 °C | 2.5 | 31.9 | −0.0675 |
| | 5 | 65.5 | −0.0632 |
| | 7.5 | 81.1 | −0.0911 |
| | 10 | 214.7 | −0.1201 |
| As-received, 4 °C | 2.5 | 382.0 | 0.2418 |
| | 5 | 234.8 | 0.1937 |
| | 7.5 | 305.4 | 0.1668 |
| | 10 | 426.0 | 0.1671 |
| Milled, 37 °C | 2.5 | 38.0 | 0.0239 |
| | 5 | 77.3 | −0.0287 |
| | 7.5 | 259.9 | 0.2017 |
| | 10 | 159.2 | −0.1455 |
| Milled, 4 °C | 2.5 | 24.1 | 0.0785 |
| | 5 | 74.8 | 0.1429 |
| | 7.5 | 111.7 | 0.1077 |
| | 10 | 68.3 | −0.0371 |

The flow curves were also fit to the Carreau-Yasuda model (Morrison, 2001b) given by Eq. (2), for a more rigorous analysis:

$$\frac{\eta(\dot{\gamma}) - \eta_\infty}{\eta_0 - \eta_\infty} = [1 + (\dot{\gamma}\lambda)^a]^{\frac{n-1}{a}} \quad (2)$$

where $\eta_\infty$ is the viscosity at high shear rates, $\eta_0$ is the viscosity at low shear rates, $\lambda$ and $a$ are fitting parameters, and $n$ is a power-law parameter that has the same definition detailed above. The parameter $\lambda$ denotes a time constant for the fluid that determines the value of $\dot{\gamma}$ at which the transition from the zero shear-rate plateau to the power-law region occurs. The value of $a$ has no physical meaning; it affects the sharpness of the curve in the aforementioned transition. The flow curve results were fit to the model for all five parameters, with the fitting lines superimposed on experimental results (Fig. 4), and the parameter values for each case tabulated in Table 4. In general, these fits have a strong correlation to the experimental data in all the cases, with minor deviations at larger $\dot{\gamma}$. In all cases, $n < 1$ and are similar to the $n$ values

**Table 4**
Carreau-Yasuda model was fit to the experimental data shown in Fig. 4, and the five model parameters tabulated. The overall model fits to the experimental data were significant in each case ($p < 0.001$) and all the model parameters were also significant ($p < 0.05$).

| Condition | $\phi$ (wt. %) | $a$ | $\lambda$ (s) | $n$ | $\eta_0$ (Pa s) | $\eta_\infty$ (Pa.s) |
|---|---|---|---|---|---|---|
| As-received, 37 °C | 2.5 | 5.5 | 246.3 | −0.0678 | 11,491 | 4 |
| | 5 | 3.9 | 268.7 | −0.1084 | 27,153 | 9 |
| | 7.5 | 4.6 | 303.7 | −0.1443 | 45,623 | 13 |
| | 10 | 1.5 | 182.4 | −0.3708 | 119,661 | 25 |
| As-received, 4 °C | 2.5 | 4.3 | 306.1 | 0.2276 | 30,235 | 3 |
| | 5 | 6.3 | 310.6 | 0.1664 | 25,484 | 15 |
| | 7.5 | 6.4 | 273.5 | 0.1652 | 33,002 | 16 |
| | 10 | 4.5 | 348.2 | 0.1569 | 57,071 | 18 |
| Milled, 37 °C | 2.5 | 5.8 | 291.9 | −0.0014 | 10,174 | 2 |
| | 5 | 3.8 | 251.8 | −0.0853 | 25,652 | 7.5 |
| | 7.5 | 8.2 | 257.2 | 0.2122 | 21,477 | 15 |
| | 10 | 1.7 | 252.1 | −0.3636 | 136,724 | 25 |
| Milled, 4 °C | 2.5 | 5.2 | 212.5 | 0.0899 | 3317 | 3 |
| | 5 | 5.4 | 207.1 | 0.1683 | 6934 | 0.1 |
| | 7.5 | 3.6 | 322.0 | 0.1143 | 19,123 | 6 |
| | 10 | 6.1 | 259.0 | −0.1412 | 25,576 | 18 |

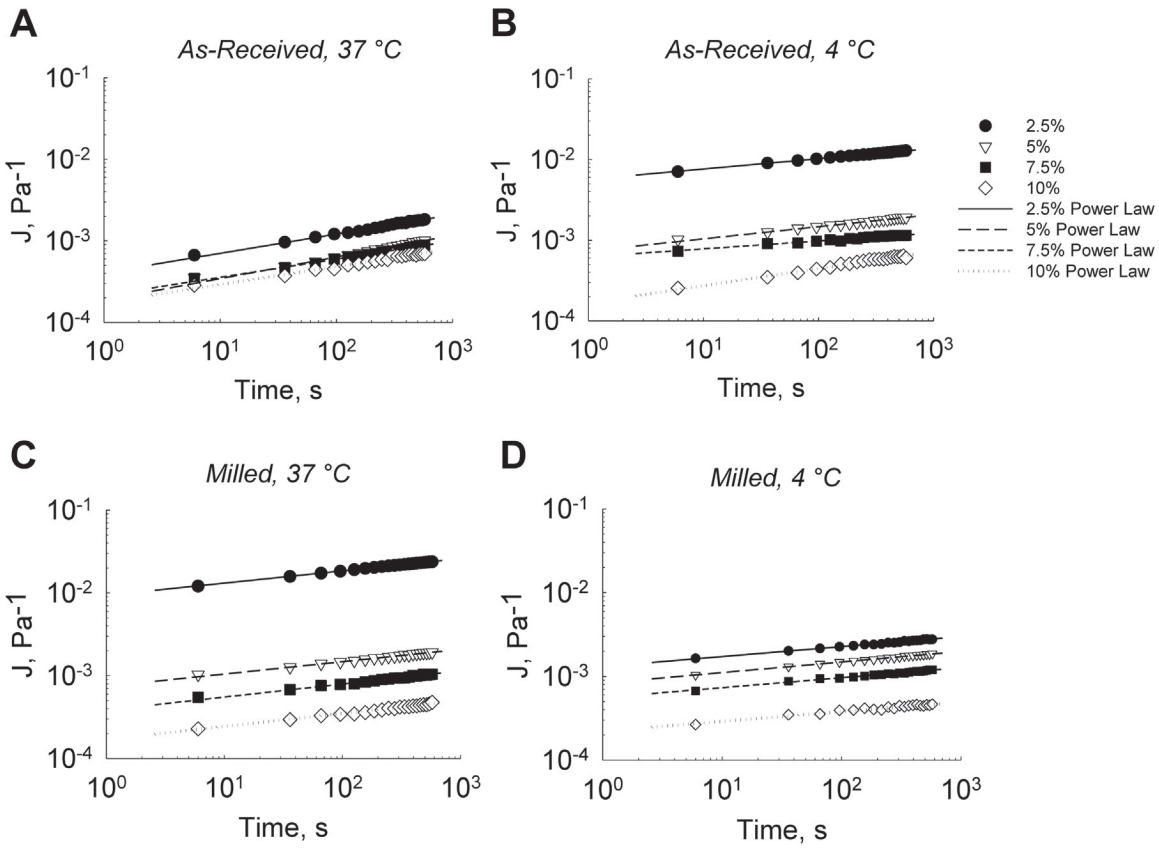


**Fig. 5.** Creep test results for the as-received powder suspensions in deionized water at 37 °C (**A**) and 4 °C (**B**), and for the milled powder suspensions in deionized water at 37 °C (**C**) and 4 °C (**D**). The experimental data (shown in open and closed symbols) were fitted with a power-law model (Eq. (3)) and the model parameters and statistical significance of the fit were shown in Table 5.

calculated from the power-law fit (Table 3). The viscosities at both low ($\eta_0$) and high ($\eta_\infty$) shear rates generally increased with $\phi$ ($p < 0.05$), which was in agreement with the graphical observations. Similar to a power-law model, the Carreau-Yasuda model is empirical and offers limited predictive power, but its greater complexity enables a better fit to the experimental data and signifies the dependence of $\eta$ on $\dot{\gamma}$.

Comparing the Carreau-Yasuda model parameters we obtained to those from literature, it was noted that these suspensions exhibited behavior typical of colloidal suspensions. Grillet et al. (2009) characterized suspensions of $Al_2O_3$ powders (average particle size ≈ 20 μm) at $0.02 \leq \dot{\gamma} \leq 2\ s^{-1}$, and found the model parameters of $a$ and $n$ to be 2.86 and 0.171, respectively. Nojoomi et al. (2014) characterized slurries of alumina and zirconia powders with particle sizes of 0.9 − 2.2 μm and 5 μm, respectively, and reported that $3.08 \leq a \leq 3.95$ and $0.2324 \leq n \leq 0.2755$, similar to those noted in our study. The values of $\eta_0$ and $\eta_\infty$ in these studies were different though, due to differences in relative magnitude of $\eta$.

### 3.5. Creep

Creep compliance was recorded against time for these suspensions (Fig. 5), and results showed that it increased with increasing $\phi$ ($p < 0.05$). This is expected because a suspension with a higher particulate content will deform less than the one with lower content, at any applied stress. The results also showed an asymptotic approach in $J$ as $t \rightarrow \infty$, which is another common observation in creep testing of suspensions (Pashkovski et al., 2003). This occurred because the suspensions yielded with the applied stress and exhibited viscous flow characteristics as it deformed over time (Kumar et al., 2012). Creep compliance $J$ could be defined as $J = 1/E = \varepsilon/\sigma$ (Juliano et al., 2007). Since $\sigma$ is constant during the creep test, $J$ is proportional to $\varepsilon$. Thus, the graphical trends found in $J$ vs. $t$ were similar to those of $\varepsilon$ vs. $t$. It could be seen from Fig. 5 that a power-law model given by Eq. (3) fits the relationship between $J$ and $t$:

$$J(t) = J_0(t/t_0)^\beta \tag{3}$$

where $t_0$ is an arbitrarily chosen time scale (typically, $t_0 = 1$ s), $J_0$ represents the creep compliance at $t = t_0$, and $\beta$ is the degree of dissipation (Ekpenyong et al., 2012). The value of $\beta$ describes the *fluidity* of the material, with $\beta = 0$ being a purely elastic material, and $\beta = 1$ being a Newtonian fluid (Chan et al., 2014). $J_0$ can provide further insight by applying the definition of $J$, yielding $E_0 = 1/J_0$ to find the apparent Young's modulus at $t = t_0$. A summary of the model fitting parameters were tabulated in Table 5.

From the power-law model fit, the values of $\beta$ were all considerably close to zero ($\beta < 0.3$), which indicates that the suspensions are poroelastic in character with viscoelastic responses, in agreement with our observations from the other rheological tests on these suspensions. For comparison, the value of $\beta$ was reported to be less than 0.45 for HL60/S4 myeloid precursor cells (Chan et al., 2014), which serves as a benchmark for the intended application to replace native tissue. The values of $J_0$ and $E_0$ pertain to the general magnitude of the curve, and results from curve-fitting indicate that the data followed the expected trend of decreased deformation with increasing $\phi$. This is evidenced by $J_0$ decreasing with increased $\phi$ ($p < 0.05$), and $E_0$ following the inverse of this trend ($p < 0.05$).

### 3.6. Stress relaxation

Fig. 6 shows the stress relaxation behavior of these particulate suspensions over time. The observed stress decayed with time at all $\phi$, for both particle types at both temperatures. Similar to results from

**Table 5**
Parameters from a power-law model fit in Eq. 3, to the experimental data from creep tests shown in Fig. 5 were tabulated. The overall model fits to the experimental data were significant in each case ($p < 0.001$) and all the model parameters were also significant ($p < 0.005$).

| Condition | $\phi$ (wt %) | $J_o$ ($Pa^{-1}$) | $\beta$ | $E_o$ (Pa) |
|---|---|---|---|---|
| As-received, 37 °C | 2.5 | 0.0004 | 0.2367 | 2500 |
| | 5 | 0.0002 | 0.2651 | 5000 |
| | 7.5 | 0.0002 | 0.2229 | 5000 |
| | 10 | 0.0002 | 0.2191 | 5000 |
| As-received, 4 °C | 2.5 | 0.0057 | 0.1282 | 175 |
| | 5 | 0.0007 | 0.1511 | 1429 |
| | 7.5 | 0.0006 | 0.0984 | 1667 |
| | 10 | 0.0002 | 0.0035 | 5000 |
| Milled, 37 °C | 2.5 | 0.0094 | 0.1477 | 106 |
| | 5 | 0.0007 | 0.1497 | 1429 |
| | 7.5 | 0.0004 | 0.1582 | 2500 |
| | 10 | 0.0002 | 0.1581 | 5000 |
| Milled, 4 °C | 2.5 | 0.0013 | 0.1193 | 769 |
| | 5 | 0.0008 | 0.1267 | 1250 |
| | 7.5 | 0.0006 | 0.1190 | 1667 |
| | 10 | 0.0002 | 0.1152 | 5000 |

creep tests, stress significantly increased with increasing $\phi$ in all cases ($p < 0.05$). The experimental data were fit to a general relaxation law (Eq. (4)) that combines Hook's law and Maxwell's law:

$$\sigma(t) = \sigma_\infty + (\sigma_0 - \sigma_\infty) \exp\left(-\frac{t}{\tau^*}\right) \quad (4)$$

where $\sigma(t)$ is the stress over time, $\sigma_0$ and $\sigma_\infty$ are the initial stress at $t = 0$ and the equilibrium stress, respectively, and $\tau^*$ is the relaxation time

**Table 6**
Stress relaxation behavior of the suspensions shown in Fig. 6 were fitted with Eq. (4) and the parameters were tabulated. The overall model fits to the experimental data were significant in each case ($p < 0.0001$) and the model parameters were also significant ($p < 0.005$).

| Condition | $\phi$ (wt%) | $\sigma_0$ (Pa) | $\sigma_\infty$ (Pa) | $\tau^*$ (s) |
|---|---|---|---|---|
| As-received, 37 °C | 2.5 | 5.48 | 2.57 | 126.8 |
| | 5 | 79.1 | 42.2 | 106.4 |
| | 7.5 | 88.2 | 42.8 | 103.5 |
| | 10 | 114.5 | 58.3 | 99.5 |
| As-received, 4 °C | 2.5 | 30.7 | 15.6 | 93.3 |
| | 5 | 46.1 | 24.3 | 108.5 |
| | 7.5 | 65.8 | 39.1 | 98.1 |
| | 10 | 139.4 | 79.7 | 111.5 |
| Milled, 37 °C | 2.5 | 16.4 | 10.6 | 114.3 |
| | 5 | 38.4 | 25.4 | 59.8 |
| | 7.5 | 48.1 | 29.2 | 102.8 |
| | 10 | 85.0 | 48.5 | 56.8 |
| Milled, 4 °C | 2.5 | 4.7 | 3.4 | 113.5 |
| | 5 | 59.3 | 38.3 | 97.3 |
| | 7.5 | 87.2 | 54.5 | 97.6 |
| | 10 | 182.2 | 114.0 | 100.1 |

(Junisbekov et al., 2003b). Stress and shear stress are interchangeable in this equation. Physically, $\tau^*$ describes the time period over which the stress has decayed to $1/e$ (i.e., 63.2%) of the difference between $\sigma_0$ and $\sigma_\infty$ (Junisbekov et al., 2003a). Table 6 shows the fitting parameters from Eq. (4) for each case tested.

The results from the stress relaxation tests suggest an increase in $\tau$ with increasing $\phi$. Since the values of $\sigma_0$ and $\sigma_\infty$ span two orders of magnitude with increasing $\phi$ ($p < 0.05$), it can be concluded that $\phi$ had a significant effect on $\tau$. To impose a given strain on a suspension, more stress is encountered with the suspensions that have higher loading.

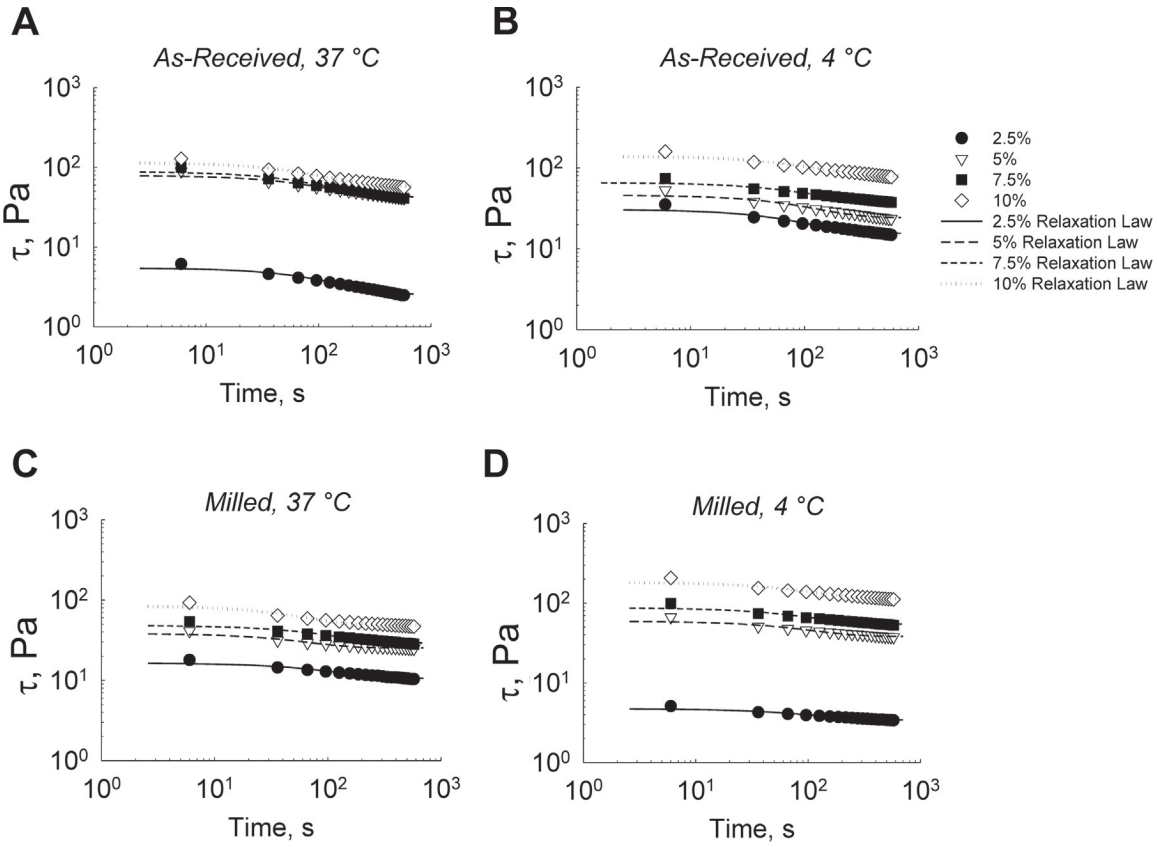


**Fig. 6.** Stress relaxation behavior of the as-received powder suspensions in deionized water at 37 °C (**A**) and 4 °C (**B**), and of milled powder suspensions in deionized water at 37 °C (**C**) and 4 °C (**D**). The experimental data (shown in open and closed symbols) were fitted with a general relaxation law (Eq. (4)) and the model parameters and statistical significance of the fit were shown in Table 6.

Thus, $\phi$ must be fine-tuned to achieve the desired mechanical properties from an applications standpoint. The lack of any apparent pattern in $\tau^*$ among various cases could possibly be due to the absence of any recoverable structure among the freely-moving particles after imposing a sufficient amount of $\tau$, leading to little governance of the timespan over which a sample relaxes. The larger relaxation times observed in the cartilage extract suspensions suggest a lack of structure after the initial deformation.

### 3.7. Maximum particulate packing density ($\phi_m$)

The relationship between the relative viscosity ($\eta_r$ = ratio of the suspension viscosity to the solvent viscosity) and $\phi$ is commonly studied in the rheological characterization of suspensions. The value of $\phi_m$ is of primary interest from an applications standpoint because it describes the theoretical upper limit on $\phi$ in a suspension. Empirical and semi-empirical models (Konijn et al., 2014) have been developed similar to the form given by $\eta_r = f(\phi; \phi_m)$, such as those by Einstein (Konijn et al., 2014), Mooney (1951), Krieger and Dougherty (1959) and Chong et al. (1971), which could be used to predict the suspension viscosity at low $\phi$ (dilute or semi-dilute suspensions) or high $\phi$ (concentrated suspensions). While this has practical value in nearly all applications involving particle suspensions, they typically require that certain parameters such as $\phi_m$ be known beforehand. A two-parameter model suggested by Liu provides an alternate way to calculate $\phi_m$ directly from $\eta$-$\phi$ data (Liu, 2000), as shown in Eq. (5):

$$\eta_r = [a(\phi_m - \phi)]^{-2} \quad (5)$$

The quantity ($\phi_m$–$\phi$) represents the space available for particles to move in the suspension. As $\phi$ approaches $\phi_m$, the term tends to zero, corresponding to infinite viscosity. The constant $a$ is the suspension-specific fitting parameter that holds no physical significance. Eq. 5 was used to determine $\phi_m$ based on studies involving highly-loaded ceramic particle suspensions (Liu, 2000). To calculate $\phi_m$ for each of the four test conditions in our study, the viscosity values at a fixed, low shear rate of 0.002 $s^{-1}$ were selected from the flow curves. Using water viscosity, the relative viscosity $\eta_r$ was calculated for each particulate loading ($\phi$ = 0, 0.025, 0.05, 0.075, and 0.1). These data were fit to Eq. (5), yielding values of $a$ and $\phi_m$, shown in Fig. 7 and Table 7.

It was noted that the value of $\phi_m$ ranges from 9 to 16.5 wt%, consistent with experimental observations. Experimentally, increasing $\phi$ to more than 15 wt% was not feasible as the suspensions turned into thick slurries that were hard to flow, much less inject. Liu reported relatively higher values of $\phi_m$ ranging from 0.41 to 0.655 for various ceramic suspensions (Liu, 2000). Alumina feedstocks with particle sizes comparable to the as-received powder have $\phi_m$ of 0.67–0.77 (Loebbecke et al., 2009). While $\phi_m$ in our study differs significantly from these reported values, our experimental observations validate the model fit calculations.

We hypothesize that the lower values of $\phi_m$ (Table 7) might be due

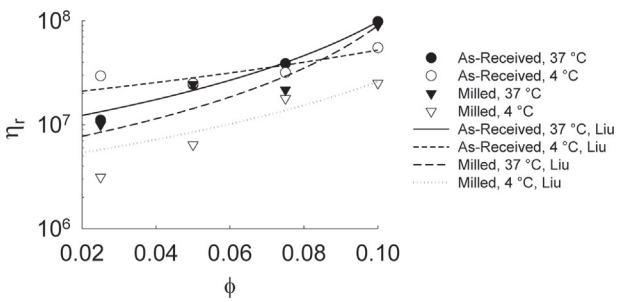


**Fig. 7.** The relative viscosities ($\eta_r$) at $\dot{\gamma}$=0.002$s^{-1}$ were plotted at each powder loading ($\phi$) tested in this study, for all the four cases. The experimental data (shown in symbols) were fitted with Liu model (Eq. (5)) and the model parameters and statistical significance of the fit were shown in Table 7.

**Table 7**
Relative viscosities ($\eta_r$) versus particle loading ($\phi$) data were fitted with Eq. (5) and the parameters were tabulated. The statistical significance of the model fit to the experimental data was also shown, with $p < 0.05$ deemed statistically significant fit.

| Condition | $\phi_m$, wt% | $a$ | $p$-value of the fit |
|---|---|---|---|
| As-received, 37 °C | 0.0902 | 0.0103 | 0.0084 |
| As-received, 4 °C | 0.1649 | 0.0014 | 0.0453 |
| Milled, 37 °C | 0.1316 | 0.0033 | 0.0031 |
| Milled, 4 °C | 0.1595 | 0.0033 | 0.0136 |

to particle flocculation (aggregates in suspensions), where the flocs themselves aren't closely packed. Zhou et al. characterized several mineral suspensions and suggested that the packing efficiency decreases when aggregates form, possibly because the particles can't arrange themselves in the optimal configuration (Zhou et al., 1995). Another potential reason for low $\phi_m$ values could be the relatively narrow particle size distributions of these particles (Fig. 1). Suspensions with broader particle size distributions typically tend to have higher values of $\phi_m$, because the smaller particles could fill the gaps between larger particles thereby enhancing the packing efficiency. Comparing the cases within our study, it is apparent that changing the particle size or temperature had no appreciable impact on $\phi_m$.

### 3.8. Proposed mechanism of particle packing in suspensions

It is important to understand the physical basis for the particulate interactions in these suspensions and propose a mechanism that depicts their rheological behavior. We first examined the relative importance of various physical phenomena that are present in this system by calculating dimensionless numbers. The Péclet number (*Pe*), given by $Pe = 6\pi\eta_0 a^3\dot{\gamma}/k_BT$, defines the ratio of forces caused by hydrodynamic interactions to those by Brownian motion, where $\eta_0$ is the viscosity of the fluid (i.e., water), $k_B$ is the Boltzmann constant, $a$ is particle radius, and $T$ is the absolute temperature (Foss and Brady, 2000; Kothapalli et al., 2008). Brownian motion dominates the flow forces when $Pe < 1$, while hydrodynamic forces dominate when $Pe > 1$. The values of *Pe* at the highest and lowest tested $\dot{\gamma}$ were shown in Table 8. While the value of *Pe* changes with $\dot{\gamma}$ through the course of the flow curve, the conditions at which $Pe = 1$ are of interest. Therefore, $\dot{\gamma}$ at $Pe = 1$ (referred to as $\dot{\gamma}^*$) for each test condition was calculated to find the point of transition between dominance of either force by rearranging the equation for *Pe*, and the results were shown in Table 8.

An interesting pattern in these calculations was that the dominant mechanism in the flow changed within the tested range of $\dot{\gamma}$ for all cases. For the as-received powder suspensions, the transition from the Brownian to the hydrodynamic regime occurred at a very low $\dot{\gamma}$, just barely greater than the lowest $\dot{\gamma}$ tested for the flow curves. This indicates that hydrodynamic interactions dominate flow characteristics over Brownian forces at almost all flow conditions. Conversely, the milled powder is governed by Brownian forces until $\dot{\gamma}$ becomes considerably larger. This key difference is due to the particle size distributions of the two powders. In the as-received powder, the large particles have enough inertia to dampen the significance of Brownian motion, so their movement is dictated by forces imparted by bulk flow. The displacement of a particle due to Brownian motion typically is inversely proportional to particle size (Jia et al., 2007), in agreement with our results. Given that the range of particle sizes exhibiting Brownian motion is sub-micron (Dhont, 1996), it is not surprising that Brownian motion is unimportant in the as-received powder except at very low $\dot{\gamma}$, as the particle sizes approach the upper bound of this range (Fig. 1). In contrast, the particles in the milled powder fall within the range typical for Brownian motion, and therefore had a significant impact on how they move (except at higher $\dot{\gamma}$). The role of temperature is diminished in comparison to particle size, but increasing the temperature slightly increased $\dot{\gamma}^*$ because Brownian motion is strengthened at higher T.

**Table 8**
Calculated values of $\dot{\gamma}^*$ and the dimensionless parameters *Pe*, $N_{EB}$, and $N_{HE}$. The values for *Pe* and $N_{HE}$ were shown at the highest and lowest $\dot{\gamma}$ tested in the flow curve experiments.

| Condition | $\dot{\gamma}^*$ ($s^{-1}$) | *Pe* | | $N_{EB}$ | $N_{HE}$ | |
|---|---|---|---|---|---|---|
| | | At lowest $\dot{\gamma}$ | At highest $\dot{\gamma}$ | | At lowest $\dot{\gamma}$ | At highest $\dot{\gamma}$ |
| As-received, 37 °C | 0.156 | $6.41\times10^{-3}$ | $6.41\times10^{1}$ | $2.01\times10^{3}$ | $3.19\times10^{-6}$ | $3.19\times10^{-2}$ |
| As-received, 4 °C | 0.062 | $1.63\times10^{-2}$ | $1.63\times10^{2}$ | $2.61\times10^{3}$ | $6.23\times10^{-6}$ | $6.23\times10^{-2}$ |
| Milled, 37 °C | 4.082 | $2.45\times10^{-4}$ | $2.45\times10^{0}$ | $3.26\times10^{2}$ | $7.51\times10^{-7}$ | $7.51\times10^{-3}$ |
| Milled, 4 °C | 1.609 | $6.22\times10^{-4}$ | $6.22\times10^{0}$ | $4.24\times10^{2}$ | $1.46\times10^{-6}$ | $1.46\times10^{-2}$ |

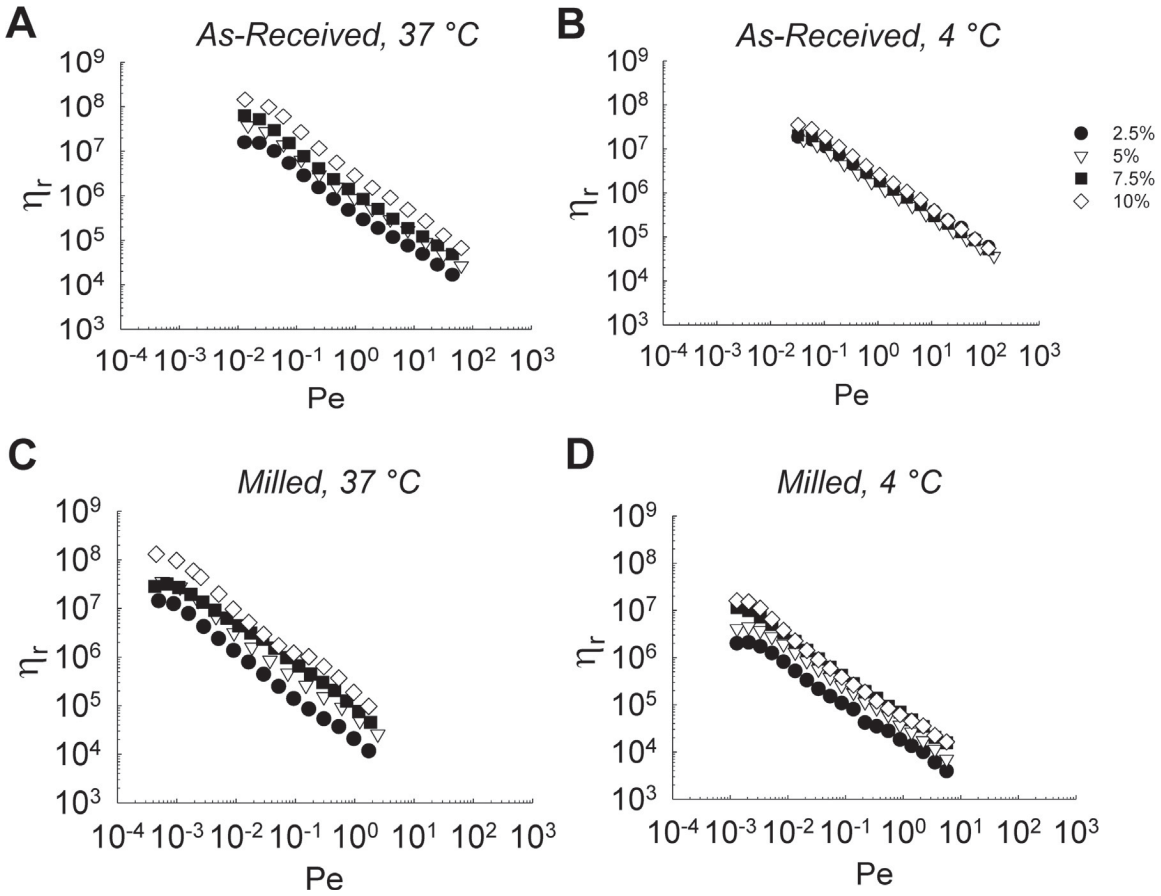


**Fig. 8.** Relative viscosities ($\eta_r$) were plotted against Péclet number for as-received powder suspensions in deionized water at 37 °C (**A**) and 4 °C (**B**), and for milled powder suspensions in deionized water at 37 °C (**C**) and 4 °C (**D**).

Fig. 8 illustrates the flow regime observed in our experiments by calculating *Pe* from the flow curve data. As *Pe* varies only with $\dot{\gamma}$ for a given particulate suspension, the only effect this had on the flow curve is a change in scale. Significant shift in $\eta_r$ - *Pe* curves were noted depending on the particle size and temperature. With increasing *Pe*, the relative importance of Brownian motion reduces, which manifests as shear-thinning in $\eta_r$.

The dimensionless number $N_{EB}$ given by $2\pi\epsilon_0\epsilon_r\psi^2 a/k_BT$ describes the ratio of electrostatic forces to Brownian forces. Here, $\epsilon_0$ and $\epsilon_r$ denote the permittivity of vacuum and the relative permittivity of the fluid, respectively, and $\psi$ is the surface potential which can be estimated as $\zeta$ (Kothapalli et al., 2008).Thus, electrostatic forces dominate if $N_{EB} > 1$, while Brownian forces dominate if $N_{EB} < 1$. The value of $N_{EB}$ was calculated for each of the four testing conditions and shown in Table 8. It could be seen that electrostatic forces were significant in all cases to varying degrees. For the as-received powder, $N_{EB}$ was especially large because Brownian forces have a weaker effect on large particles. In the milled powder, electrostatic forces were also considerably greater than Brownian forces, but to a lesser extent. As expected, $N_{EB}$ increased with decreasing T because Brownian motion was reduced.

Finally, the relationship between hydrodynamic and electrostatic forces was obtained from the expressions for *Pe* and $N_{EB}$, and defined as the ratio of hydrodynamic forces to electrostatic forces, i.e., $N_{HE} = 3\eta_0 a^2\dot{\gamma}/\epsilon_0\epsilon_r\psi^2$. The calculated $N_{HE}$ values for each test condition at the upper and lower bounds of $\dot{\gamma}$ were shown in Table 8. It was evident that $N_{HE}$«1 across all cases, so electrostatic forces play a significant role in this system under many different flow conditions.

To directly compare the magnitudes of the different types of forces against each other, we calculated the hydrodynamic ($F_H=6\pi\eta_0 a^2\dot{\gamma}$), Brownian ($F_B = k_BT/a$), and electrostatic forces ($F_E=2\pi\epsilon_0\epsilon_r\psi^2$) that a single particle experiences, respectively. The three forces were calculated across all cases and were compiled in Table 9. It could be seen that electrostatic forces were the most dominant in this system, followed by hydrodynamic forces at $\dot{\gamma} > \dot{\gamma}^*$. Brownian forces were the least important except when $\dot{\gamma} < \dot{\gamma}^*$. We again note that the smaller particles in the milled powder exhibited less resistance to flow since $F_H$ was always less than that calculated in the as-received cases. Unlike as-received powder, milled particulates exhibited larger forces due to Brownian motion since they were more easily affected by thermal agitation. The electrostatic forces differed due to a slight dependency on temperature

**Table 9**
Calculated values of the forces $F_H$, $F_B$, and $F_E$. The values for $F_H$ were calculated at the highest and lowest $\dot{\gamma}$ used in experiments.

| Condition | $F_B$ (N) | $F_H$ (N) | | $F_E$ (N) |
|---|---|---|---|---|
| | | Lowest $\dot{\gamma}$ | Highest $\dot{\gamma}$ | |
| As-received, 37 °C | $3.34\times10^{-15}$ | $2.14\times10^{-17}$ | $2.14\times10^{-13}$ | $6.70\times10^{-12}$ |
| As-received, 4 °C | $2.98\times10^{-15}$ | $4.85\times10^{-17}$ | $4.85\times10^{-13}$ | $7.78\times10^{-12}$ |
| Milled, 37 °C | $9.91\times10^{-15}$ | $2.43\times10^{-18}$ | $2.43\times10^{-14}$ | $3.23\times10^{-12}$ |
| Milled, 4 °C | $8.86\times10^{-15}$ | $5.50\times10^{-18}$ | $5.50\times10^{-14}$ | $3.76\times10^{-12}$ |

(since $\epsilon_r$ depends on T), but the main reason could be attributed to the differences in the zeta potentials of the two powder types. It is apparent that future work should investigate the effectiveness of stabilizers and surfactants on these particulate suspensions as electrostatic forces are the strongest in this system.

Based on our experimental results and this analysis, we hypothesize that the particles formed a structure that initially exhibited poroelastic characteristics ($G' > G\hexagon$), as noted from the amplitude and frequency sweep data. As the suspension was sheared, it resisted motion at very low $\dot{\gamma}$ until it yielded and broke down to enable flow (peak in $\eta$ at $\dot{\gamma}$=0.002 $s^{-1}$). The particulate clusters in the suspension might not have completely broken down into individual particles, but instead progressively broke down into smaller clusters with increasing $\dot{\gamma}$. This phenomenon, often referred to as rheofluidization, is responsible for shear-thinning observed in particulate suspensions (Perez et al., 2000) as well as hydrogels (Yan et al., 2010). The sample acted more fluid-like with increased shearing due to the presence of smaller clusters, as seen in amplitude sweep results where $G'$ eventually became less than $G\hexagon$ as $\gamma$ increased in all cases.

Our observation that the viscosity of milled powder suspensions was always lower than that for the as-received powder suspensions could be explained by a more favorable packing of agglomerates in the milled powder, which were mostly smaller than those found in the as-received powder. This contributed to less resistance to shear and lower overall viscosity. The reason for the smaller agglomerates is explained by the physical nature of the particles itself, and the forces they encountered during experiments. Brownian forces have a more significant impact on these particles, inducing enough vibration to deter the formation of larger aggregates. This did not occur to the same extent in the as-received powder, so aggregates were larger with lower packing efficiency, resulting in higher viscosities. The rheological characterization results presented here will be repeated in a future study using a different batch of chicken sternal cartilage extract to account for batch to batch variation, if any, and ensure reproducibility of these conclusions. Our current experiments are designed to test these hypotheses, optimize the solvent medium, and identify the effects of thermodynamically-compatible biopolymers which could help stabilize these suspensions by modulating their viscoelastic properties.

Biodegradable collagen-based products (e.g., NeoCart®, NovoCART®3D, CaReS®, Chondro-Gide®, Maioregen®) to regenerate or treat degraded cartilage have been developed for clinical applications. These products are typically gel or suspension based formulations and having a detailed knowledge of their rheological properties, such as those investigated in this study, is critical for stable formulation development, large-scale manufacturing, storage and shipment, preclinical handling, and effective clinical delivery at the affected region in patients. Although the viscosity of suspensions depends on the shear rate at which it is measured, the reversible aggregation of chicken sternal cartilage extract powders in our study seem to largely depend on inter-particle interactions for the loading amounts tested here. Results suggest that these particles tend to form aggregates at low flow rates or under standstill conditions and more shear stress is needed to break up the agglomerates at low shear rates, similar to that noted in red blood cell rheology. Finally, the viscosity and yield stress of these suspensions could be further manipulated by introducing hydrocolloids or synthetic polymers (e.g., guar gum, polyacrylics) for better suitability in clinical settings.

## 4. Conclusions

The rheological properties of unhydrolyzed chicken sternal cartilage extract powder in aqueous suspensions were investigated to establish the baseline characteristics and determine its suitability for cartilage replacement applications. Results from amplitude and frequency sweep data indicated that the suspensions are more elastic than viscous in all cases. The flow curves indicated that the particulate suspensions exhibited shear-thinning behavior typical of numerous colloidal suspensions, though the maximum powder loading is lower than suspensions of comparable particle sizes. The creep and stress relaxation results demonstrated that the suspensions tend toward poroelastic behavior and confirm that their material properties are significantly impacted by the amount of powder loading, and to a lesser extent, by temperature. Further analysis showed that electrostatic forces have a relatively strong influence on particle interactions and suspension properties by extension. Based on the results and analysis, a general model describing the physical behavior of these particles in suspension was postulated, assuming the presence of a structure that forms at rest and yields under shear. Taken together, with some fine-tuning of the formulations, these suspensions could exhibit qualities desirable in cartilage-mimicking materials.

## Acknowledgements

Brian Hama was an undergraduate student when he performed this research and gratefully acknowledges the support from Jack, Joseph, and Morton Mandel Honors College at CSU. This work was partially supported by the Summer Undergraduate Research funds from CSU Office of Research and by the National Science Foundation (CBET) grant number 1337859 to C.K. Experimental assistance from Dr. Kurt Farrell and discussions with Dr. Chris Wirth is also appreciated.

## References

Abdelhamid, E., Elaissari, E., 2003. Colloidal Biomolecules, Biomaterials, and Biomedical Applications. Taylor & Francis.
Alkayali, A., 2000. Hydrolyzed collagen type II and use thereof, in: US08/907735 (Ed.).
Alkayali, A., 2001. Method of making hydrolyzed collagen type II, in: US09453302 (Ed.).
Burns, N.A., Naclerio, M.A., Khan, S.A., 2014. Nanodiamond gels in nonpolar media: colloidal and rheological properties. J. Rheol. 58, 1599–1614.
Chan, C.J., Whyte, G., Boyde, L., Salbreux, G., Guck, J., 2014. Impact of heating on passive and active biomechanics of suspended cells. Interface Focus 4, 1–11.
Chen, P., Zhu, S., Wang, Y., Mu, Q., Wu, Y., Xia, Q., Zhang, X., Sun, H., Tao, J., Hu, H., Lu, P., 2014. The amelioration of cartilage degeneration by ADAMTS-5 inhibitor delivered in a hyaluronic acid hydrogel. Biomaterials 35, 2827–2836.
Chong, J.S., Christiansen, E.B., Baer, A.D., 1971. Rheology of concentrated suspensions. J. Appl. Polym. Sci. 15, 2007–2021.
Clogston, J.D., Patri, A.K., 2011. Zeta potential measurement. Methods Mol. Biol. 697, 63–70.
Dhont, J.K.G., 1996. An Introduction to Dynamics of Colloids. Elsevier, Amsterdam, The Netherlands.
Ekpenyong, A.E., Whyte, G., Chalut, K., Pagliara, S., Lautenschläger, F., Fiddler, C., Paschke, S., Keyser, U.F., Chilvers, E.R., Guck, J., 2012. Viscoelastic properties of differentiating blood cells are fate- and function-dependent. PLoS One 7, 1–10.
Foss, D.R., Brady, J.F., 2000. Structure, diffusion and rheology of Brownian suspensions by Stokesian dynamics simulation. J. Fluid Mech. 407, 167–200.
Foudazi, R., Nazockdast, H., 2012. Rheology and morphology of nanosilica-containing polypropylene and polypropylene/liquid crystalline polymer blend. J. Appl. Polym. Sci. 128, 3501–3511.
Freymann, U., Endres, M., Neumann, K., Scholman, H.J., Morawietz, L., Kaps, C., 2012. Acta Biomater. 8, 677–685.
Fulcher, G.R., Hukins, D.W., Shepherd, D.E., 2009. Viscoelastic properties of bovine articular cartilage attached to subchondral bone at high frequencies. BMC Musculoskelet. Disord. 10, 61–68.
Gobeaux, F., Belamie, E., Mosser, G., Davidson, P., Asnacios, S., 2010. Power law rheology and strain-induced yielding in acidic solutions of type I-collagen. Soft Matter 6, 3769–3777.
Grillet, A.M., Rao, R.R., Adolf, D.B., Kawaguchi, S., Mondy, L.A., 2009. Practical application of thixotropic suspension models. J. Rheol. 53, 169–189.

Harris, I.R., Harmon, A.M., Brown, L.J., Gosiewska, A., 2011. Tissue-engineering scaffolds containing self-assembled-peptide hydrogels, in: US10/951357 (Ed.).
Ishaq, S., 2006. Hyaluronic acid and chondroitin sulfate based hydrolyzed collagen type II and method of making same, in: US10/870841 (Ed.).
Jeong, B., Lee, K.M., Gutowska, A., An, Y.H., 2002. Thermogelling biodegradable copolymer aqueous solutions for injectable protein delivery and tissue engineering. Biomacromolecules 3, 865–868.
Jia, D., Hamilton, J., Zaman, L.M., Goonewardene, A., 2007. The time, size, viscosity, and temperature dependence of the Brownian motion of polystyrene microspheres. Am. J. Phys. 75, 111–115.
Juliano, T.F., VanLandingham, M.R., Tweedie, C.A., Van Vliet, K.J., 2007. Multiscale creep compliance of epoxy networks at elevated temperatures. Exp. Mech. 47, 99–105.
Junisbekov, T.M., Kestelman, V.N., Malinin, N.I., 2003a. Determination of Relaxation Characteristics, Stress Relaxation in Viscoelastic Materials. Science Publishers, Inc., Enfield, NewHampshire, pp. 91–133.
Junisbekov, T.M., Kestelman, V.N., Malinin, N.I., 2003b. Foundations of the Theory of Stress Relaxation, Stress Relaxation in Viscoelastic Materials. Science Publishers, Inc., Enfield, NewHampshire, pp. 1–90.
Kadajji, V.G., Betageri, G.V., 2011. Water soluble polymers for pharmaceutical applications. Polymers 3, 1972–2009.
Kim, K.S., Park, S.J., Yang, J.A., Jeon, J.H., Bhang, S.H., Kim, B.S., Hahn, S.K., 2011. Injectable hyaluronic acid–tyramine hydrogels for the treatment of rheumatoid arthritis. Acta Biomater. 7, 666–674.
Kitazono, E., Kaneko, H., Ito, M., Fukutomi, C., Tsuzuki, S., Sumi, Y., 2008. Hyaluronic Acid Compound, Hydrogel Thereof and Joint Treating Material, in: PCT/JP2004/016285 (Ed.).
Klouda, L., Mikos, A.G., 2008. Thermoresponsive hydrogels in biomedical applications. Eur. J Pharm. Biopharm. 68, 34–45.
Klüver, E., Meyer, M., 2012. Preparation, processing, and rheology of thermoplastic collagen. J. Appl. Polym. Sci. 128, 4201–4211.
Konijn, B.J., Sanderink, O.B.J., Kruyt, N.P., 2014. Experimental study of the viscosity of suspensions: effect of solid fraction, particle size and suspending liquid. Powder Technol. 266, 61–69.
Korhonen, R.K., Laasanen, M.S., Toyras, J., Lappalainen, R., Helminen, H.J., Jurvelin, J.S., 2003. Fibril reinforced poroelastic model predicts specifically mechanical behavior of normal, proteoglycan depleted and collagen degraded articular cartilage. J. Biomech. 36, 1373–1379.
Kothapalli, C.R., Wei, M., Shaw, M.T., 2008. Solvent-specific gel-like transition via complexation of polyelectrolyte and hydroxyapatite nanoparticles suspended in water-glycerin mixtures; a rheological study. Soft Matter 4, 600–605.
Krieger, I.M., Dougherty, T.J., 1959. A mechanism for Non-Newtonian flow in suspensions of rigid spheres. J. Rheol. 3, 137–152.
Krishnaswamy, R., Kalyanikutty, K.P., Biswas, K., Sood, A.K., Rao, C.N.R., 2009. Viscoelastic properties of nanocrystalline films of semiconducting chalcogenides at liquid/liquid interface. Lagmuir 25, 10954–10961.
Kumar, A., Stickland, A.D., Scales, P.J., 2012. Viscoelasticity of coagulated alumina suspensions. Korea Aust. Rheol. J. 24, 105–111.
Li, Y., Rodrigues, J., Tomás, H., 2012. Injectable and biodegradable hydrogels: gelation, biodegradation and biomedical applications. Chem. Soc. Rev. 41, 2193–2221.
Liu, D.M., 2000. Particle packing and rheological property of highly-concentrated ceramic suspensions: $\varphi_m$ determination and viscosity prediction. J. Mater. Sci. 35, 5503–5507.
Loebbecke, B., Knitter, R., Haubelt, J., 2009. Rheological properties of alumina feedstocks for the low-pressure injection moulding process. J. Eur. Ceram. Soc. 29, 1595–1602.
Ma, P., Langer, R., 1999. Morphology and mechanical function of long-term in vitro engineered cartilage. J. Biomed. Mater. Res. 44, 217–221.
Mononen, M.E., Julkunen, P., Töyräs, J., Jurvelin, J.S., Kiviranta, I., Korhonen, R.K., 2011. Alterations in structure and properties of collagen network of osteoarthritic and repaired cartilage modify knee joint stresses. Biomech. Model Mechanobiol. 10, 357–369.
Mooney, M., 1951. The viscosity of a concentrated suspension of spherical particles. Colloid Sci. 6, 162–170.
Morrison, F.A., 2001a. Rheometry. In: Grubbins, K.F. (Ed.), Understanding Rheology. Oxford University Press, New York, NY, pp. 454.
Morrison, F.A., 2001b. Generalized Newtonian fluids. In: Grubbins, K.F. (Ed.), Understanding Rheology. Oxford University Press, New York, NY, pp. 225–256.
Mow, V., Holmes, M., Lai, W., 1984. Fluid transport and mechanical properties of articular cartilage: a review. J. Biomech. 17, 377–394.
Nojoomi, A., Faghihi-Sani, M.A., Khoshkalam, M., 2014. Shear-rate dependence modeling of gelcast slurries: effects of dispersant content and solid loading. Ceram. Int. 40, 123–128.
Olhero, S.M., Ferreria, J.M.F., 2004. Influence of particle size distribution on rheology and particle packing of silica-based suspensions. Powder Technol. 139, 69–75.
Pashkovski, E.E., Masters, J.G., Mehreteab, A., 2003. Viscoelastic scaling of colloidal gels in polymer solutions. Lagmuir 19, 3589–3595.
Perez, M., Barbé, J.C., Neda, Z., Bréchet, Y., Salvo, L., 2000. Computer simulation of the microstructure and rheology of semi-solid alloys under shear. Acta Mater. 48, 3773–3782.
Pham, K.N., Petekidis, G., Vlassopoulos, D., Egelhaaf, S.U., Pusey, P.N., Poon, W.C.K., 2006. Yielding of colloidal glasses. Europhys. Lett. 75, 624–630.
Polachini, T.C., Sato, A.C.K., Cunha, R.L., Telis-Romero, J., 2016. Density and rheology of acid suspensions of peanut waste in different conditions: an engineering basis for bioethanol production. Powder Technol. 294, 168–176.
Prasad, D., Kytömaa, H.K., 1995. Particle stress and viscous compaction during shear of dense suspensions. Int. J. Multiph. Flow. 21, 775–785.
Purslow, P.P., Wess, T.J., Hukins, D.W., 1997. Collagen orientation and molecular spacing during creep and stress-relaxation in soft connective tissues. J. Exp. Biol. 201, 135–142.
Reddi, A.H., Becerra, J., Andrades, J.A., 2011. Nanomaterials and hydrogel scaffolds for articular cartilage regeneration. Tissue Eng. Part B Rev. 17, 301–305.
Saravacos, G.D., 1970. Effect of temperature on viscosity of fruit juices and purees. J. Food Sci. 35, 122–125.
Sheu, S.Y., Chen, W.S., Sun, J.S., Lin, F.H., Wu, T., 2013. Biological characterization of oxidized hyaluronic acid/resveratrol hydrogel for cartilage tissue engineering. J. Biomed. Mater. Res A 101, 3457–3466.
Shi, Y., Zhang, Y., 2008. Simulation of random packing of spherical particles with different size distributions. Appl. Phys. A 92, 621–626.
Shukla, A., Arnipally, S., Dagaoknar, M., Joshi, Y.M., 2015. Two-step yielding in surfactant suspension pastes. Rheol. Acta 54, 353–364.
Stainmesse, S., Orecchioni, A.M., Nakache, E., Puisieux, F., Fessi, H., 1995. Formation and stabilization of a biodegradable polymeric colloidal suspension of nanoparticles. Colloid. Polym. Sci. 273, 505–511.
Stiles, T., 2002. Kolla2-desiccated avian sternal cartilage powder, in: US09/768141 (Ed.).
Sze, A., Erickson, D., Ren, L., Li, D., 2003. Zeta-potential measurement using the Smoluchowski equation and the slope of the current–time relationship in electroosmotic flow. J. Colloid Interface Sci. 261, 402–410.
Ulery, B.D., Nair, L.S., Laurencin, C.T., 2011. Biomedical applications of biodegradable polymers. J. Polym. Sci. B Polym. Phys. 49, 832–864.
Vand, V., 1948. Viscosity of solutions and suspensions II: experimental determination of the viscosity-concentration function of spherical suspensions. J. Phys. Colloid Chem. 52, 300–314.
Vouland, E., Berger, C., 2010. Hydrolysate of avian cartilage, process of preparation and uses thereof, in: PCT/EP2007/053850 (Ed.).
Waldstein, W., Perino, G., Gilbert, S.L., Maher, S.A., Windlhager, R., Boettner, F., 2016. OARSI osteoarthritis cartilage histopathology assessment system: a biomechanical evaluation in the human knee. J. Orthop. Res. 34, 135–140.
Yan, C., Altunbas, A., Yucel, T., Nagarkar, R.P., Schneider, J.P., Pochan, D.J., 2010. Injectable solid hydrogel: mechanism of shear-thinning and immediate recovery of injectable β-hairpin peptide hydrogels. Soft Matter 6, 5143–5156.
Zhou, J.Z.Q., Fang, T., Luo, G., Uhlherr, P.H.T., 1995. Yield stress and maximum packing fraction of concentrated suspensions. Rheol. Acta 34, 544–561.